



Investigation of the physical properties of $(\text{Cu}_{0.5}\text{Tl}_{0.5})\text{Ba}_2\text{Ca}_2\text{Cu}_3\text{O}_{10-\delta}$ impregnated with mono cobalt(II)-substituted Undecatungstosilicate Nanoparticles

Abbass Nasser¹ · Ali Srour¹ · Nour El Ghouch² · Walid Malaeb¹ · Rami Al-Oweini³ · Ramadan Awad¹

Received: 18 June 2020 / Accepted: 16 October 2020 / Published online: 23 November 2020
© Springer-Verlag GmbH Germany, part of Springer Nature 2020

Abstract

A series of $(\text{Cu}_{0.5}\text{Tl}_{0.5})\text{Ba}_2\text{Ca}_2\text{Cu}_3\text{O}_{10-\delta}$ superconducting samples impregnated with different percentage additions of potassium salt $\{\text{CoSiW}_{11}\}_x$ nanoparticles ($x = 0.00, 0.01, 0.02, 0.04, 0.06, 0.08$ and 0.12 wt.%) were prepared using a single-step solid-state reaction technique at ambient pressure. These samples were characterized by powder X-ray diffraction (XRD), scanning electron microscopy (SEM) and energy-dispersive X-ray spectroscopy (EDX) to study their structures, construction of the synthesized samples and elemental composition, respectively. XRD studies indicate that the tetragonal structure of $(\text{Cu}_{0.5}\text{Tl}_{0.5})$ -1223 phase has not changed by the addition of $\{\text{CoSiW}_{11}\}$ nanoparticles the same as for the values of lattice parameters a and c , where they show a non-remarkable change. The relative volume fraction of (CuTl) -1223 phase record a maximum value for $x = 0.02$ wt.%. The formation of (CuTl) -1223 phase matches the presence of rectangular-shaped plates seen in SEM images. The enhancement of these plates after the addition of $\{\text{CoSiW}_{11}\}$ nanoparticles up to $x = 0.02$ wt.% agreed with the measurements of relative volume fraction. The mass percentage of all elements was measured using the EDX technique, which shows the distribution composition of both superconductor and nanoparticle compounds. Vibrational mode analyses of oxygen were accomplished via Fourier transform infrared (FTIR) spectroscopy in (CuTl) -1223 phase impregnated with $\{\text{CoSiW}_{11}\}$ nanoparticles. The O_δ oxygen modes observed are almost unaltered while the other oxygen modes of planar CuO_2 are slightly softened and hardened. Superconducting transition temperature (T_c) and critical current density (J_c) were determined from the electrical resistivity and I - V measurements, respectively. The results indicate an increase in the T_c values from 125 K for the pure sample to 132 K for $x = 0.02$ wt.% impregnated samples, while a decrease in the J_c values is observed upon increasing 'x' value from $x = 0.00$ up to 0.12 wt.%. The suppression of these electrical superconducting parameters for $x > 0.02$ wt.% may be due to an increase of weak links' connectivity among the grain boundaries and growth of impurity phases that affect the formation of (CuTl) -1223 superconductor phase. The fluctuation-induced conductivity (FIC) analysis has been done in the light of the Aslamasov–Larkin (AL) theory to study the fluctuation conductivity $\Delta\sigma$ above T_c as a function of reduced temperature for $(\text{CoSiW}_{11})_x/(\text{CuTl})$ -1223 superconductor. The results show four non-identical fluctuation regions that are short-wave (Sw), two-dimensional (2D), three-dimensional (3D) and critical (Cr). The zero-temperature coherence length ($\xi_c(0)$), the effective layer thickness of the two-dimensional system (d), inter-layer coupling (I), Fermi velocity (v_F) and Fermi energy (E_F) were evaluated as a function of 'x' addition from FIC analysis of the samples and then correlated to the superconductivity order parameters. The superconducting parameters were increased upon the addition of $\{\text{CoSiW}_{11}\}$ nanoparticles.

Keywords (CuTl) -1223 superconductor · Polyoxometalates · FTIR · Excess conductivity

1 Introduction

Since the discovery of high-temperature superconductors (HTSCs), many researches have made serious efforts to ameliorate their critical parameters and transport properties to enhance the technological applications and techniques [1]. $(\text{Cu}_{0.5}\text{Tl}_{0.5})\text{Ba}_2\text{Ca}_2\text{Cu}_3\text{O}_{10-\delta}$ phase is one of the most

✉ Walid Malaeb
w.malaeb@bau.edu.lb

Extended author information available on the last page of the article

attractive superconductor phases of HTSCs cuprates due to its high values of superconducting transition temperature (T_c), the critical current density (J_c) the zero-temperature coherence length $[\xi(0)]$ [2, 3]. An interesting property of this phase is the preparation at ambient pressure [4]; this is because it is a simple, time-saving and cost-effective process. Its unit cell structure is composed of an isolating charge reservoir layer, $\text{Cu}_{0.5}\text{Tl}_{0.5}\text{Ba}_2\text{O}_{4.6}$, and three CuO_2 planes interceded by Ca atoms [5].

The studies of excess conductivity are regarded as an important tool, focusing on the transport properties of HTSCs close to the transition region and beyond. The excess conductivity or fluctuation-induced conductivity (FIC), $\Delta\sigma(T)$, is widely studied for various superconducting compounds [6, 7]. The Aslamazov–Larkin (AL) model fits well for thin films as does the Lawrence–Doniach (LD) model in bulk superconductors [8, 9]. A study of fluctuation-induced excess conductivity in the MgB_2 sample by Rajput [10], with (AL) model and (LD) model indicates the three-dimensional nature of conduction of the carriers as opposed to the 2D character exhibited by the HTSCs and he found that the coherence length is $\sim 21 \text{ \AA}$ from (AL) model, same as found by other authors.

The incorporation of nanostructured materials in bulk HTSCs is an effective way to enhance the transport properties [11] and the additional pinning effects in the bulk polycrystalline samples result in the improvement of in-field superconducting properties. Many attempts have been made to reduce the inter-grain voids and fill the pores and empty nano-scale spaces [12]. Additionally, several studies were carried out to investigate the influence of nanoparticle addition for various superconducting phases [7, 13–17]. For instance, it was observed that the low concentration of nano-ZnO addition in $(\text{Cu}_{0.5}\text{Tl}_{0.25}\text{Pb}_{0.25})$ -1223 matrix improved the superconducting properties (J_c , T_c and the volume fraction), while high concentrations increased the grain-boundaries' resistance due to agglomeration of nano-ZnO particles [13]. Mumtaz et al. [14] found that adding the nano-particle $(\text{DNP})_x$ to $(\text{Cu}_{0.5}\text{Tl}_{0.5})$ -1223 increased T_c for $x=0.5$ wt.% and improved the inter-grain connectivity of (CuTi) -1223 phase. Furthermore, the addition of Ni nanoparticles into $(\text{Cu}_{0.5}\text{Tl}_{0.5})$ -1223 phase reduced the superconducting volume fraction, resulting in a shift in the 3D conductivity and a decrease in the interlayer coupling ' T ' and ' $\xi_c(0)$ ' [8]. Mohammed et al. [7] displayed the effect of Ti substitution into $(\text{Cu}_{0.5}\text{Tl}_{0.5})$ -1223 phase, revealing that the increment of 3D width as Ti substitution increased, thus improving the mobility of free charge transporters in three dimensions and decreasing the value of the lattice parameter c .

On the other hand, polyoxometalates (POMs) are inorganic nanoparticles of metal oxides clusters, which are considered as highly agreeable materials regarding their structural properties, reactivity and relevance. Thus, they are

useful for many applications such as in medicine, catalysis, and materials science [18–24]. To the best of our knowledge, very few studies have been carried on the influence of POM nanoparticles on superconductor properties. El Ghouh et al. [25, 26] investigated the addition of $\{\text{FeSiW}_{11}\}$ and $\{\text{MnSiW}_{11}\}$ POM nanoparticles on (Bi,Pb) -2223 superconductor phase. The reports revealed that the addition of $\{\text{MnSiW}_{11}\}$ and $\{\text{FeSiW}_{11}\}$ nanoparticles enhanced the volume fraction, T_c and J_c of (Bi,Pb) -2223 phase.

The present work aims at investigating the effect of the phase formation and inter-grains connectivity, as well as T_c , J_c and the excess conductivity of the $(\text{Cu}_{0.5}\text{Tl}_{0.5})$ -1223 phase. For this purpose, seven samples of $(\text{CoSiW}_{11})_x/(\text{Cu}_{0.5}\text{Tl}_{0.5})$ -1223, $0.00 \leq x \leq 0.12$ wt.%, were prepared using a conventional solid-state reaction technique. The different samples were structurally characterized using powder X-ray diffraction (XRD), energy-dispersive X-ray spectroscopy (EDX), scanning electron microscopy (SEM) and Fourier transform infrared (FTIR) analysis. Also, the dc-electrical resistivity, critical current density and excess conductivity measurements were performed to obtain the transport properties of $(\text{CoSiW}_{11})_x/(\text{Cu}_{0.5}\text{Tl}_{0.5})$ -1223 superconductor phase samples.

2 Materials and methods

2.1 Materials

The chemicals used in the preparation of POM nanoparticles are cobalt nitrate ($(\text{Co}(\text{NO}_3)_2 \cdot 6\text{H}_2\text{O}, \geq 99\%)$, sodium metasilicate ($\text{Na}_2\text{SiO}_3 \cdot 5\text{H}_2\text{O}, \geq 95\%$) and sodium tungstate ($\text{Na}_2\text{WO}_4 \cdot 2\text{H}_2\text{O}, \geq 95\%$), purchased from SIGMA-ALDRICH and HIMEDIA, respectively, and used without further purification. Moreover, distilled water, acquired and prepared in the lab via RO water distiller, was used as a solvent. As for the superconductor phase, the analytical grade of calcium oxide powder ($\text{CaO}, \geq 95\%$) was used from HIMEDIA, while thallium (III) oxide ($\text{Tl}_2\text{O}_3, 99\%$), barium peroxide ($\text{BaO}_2, \geq 95\%$), copper (II) oxide ($\text{CuO}, 98\%$) were used from SIGMA-ALDRICH.

2.2 Synthesis of POM nanoparticles and characterizations

The $\{\text{CoSiW}_{11}\}$ nanoparticles were synthesized according to Müller et al. [27]. Typically, 5 mL distilled water was used to dissolve a solution of 0.146 g cobalt nitrate ($\text{Co}(\text{NO}_3)_2 \cdot 6\text{H}_2\text{O}, 0.5 \text{ mmol}$), and then the obtained solution was heated until boiling. A sample of 1.61 g of the solid $(\text{K}_8[\alpha\text{-SiW}_{11}\text{O}_{39}] \cdot 13\text{H}_2\text{O}, 0.5 \text{ mmol})$ was added in small amounts over 10 min to the boiling solution. The process of preparing $(\text{K}_8[\alpha\text{-SiW}_{11}\text{O}_{39}] \cdot 13\text{H}_2\text{O})$ is reported in

the literature [27]. After filtering this solution, a 0.2-g of potassium chloride (KCl, 2.7 mmol) was prepared by dissolving in 1 mL distilled water and added to the final solution. The mixture was then placed at 278 K for 2 days in the refrigerator. The $[\text{Co}^{\text{II}}\text{SiW}_{11}(\text{H}_2\text{O})\text{O}_{39}] \cdot 14\text{H}_2\text{O} \{ \text{CoSiW}_{11} \}$ nanoparticles were filtered out and finally air-dried.

XRD was used to investigate the structural properties of the nanoparticles with $\text{Cu-K}\alpha$ radiation on a Bruker D8 Advance powder diffractometer. Transmission electron microscopy (TEM), JEM-100CX, was used to determine the crystalline size and the surface morphology of $\{ \text{CoSiW}_{11} \}$, which proceeded at 80 kV. Besides, FTIR spectroscopy was used to characterize the nanoparticles in the range $2000\text{--}550\text{ cm}^{-1}$, using a Nicolet iS5 spectrometer.

2.3 Preparation of superconductor samples

$(\text{Cu}_{0.5}\text{Tl}_{0.5})\text{Ba}_2\text{Ca}_2\text{Cu}_3\text{O}_{10-\delta}$ superconductor samples impregnated with different percentages of $\{ \text{CoSiW}_{11} \}$ POM nanoparticles varied from $x=0.00\text{ wt.}\%$ to $0.12\text{ wt.}\%$ were prepared by a single-step solid-state reaction method. First, stoichiometric quantities of BaO_2 , CaO , CuO and Tl_2O_3^* were weighted and then blended well. The obtained mixture was grinded in an agate mortar into a fine powder and then sifted using a sieve ($60\text{ }\mu\text{m}$) to obtain a homogenous mixture. The POM nanoparticles with different wt.% amounts were added into the mixed compound. Afterward, the powder was compressed to 13 mm-diameter discs under 11 tons (for 2 min) and then the obtained discs were wrapped with a silver foil, preventing the mass loss of thallium during the heating process. The sample was then introduced in a sealed quartz tube of length 10 cm and diameter 3 cm and put in a computerized box furnace (Gallenkamp, FSL-340-110w). The heating process started with a rate of $4\text{ }^\circ\text{C}/\text{min}$ up to $740\text{ }^\circ\text{C}$ and $2\text{ }^\circ\text{C}/\text{min}$ up to $845\text{ }^\circ\text{C}$, which was left for 4 h. Finally, a cooling rate of about $2\text{ }^\circ\text{C}/\text{min}$ was applied to decrease its temperature back to room temperature.

2.4 Crystal structure and morphology characterization

The prepared samples $(\text{CoSiW}_{11})_x/(\text{Cu}_{0.5}\text{Tl}_{0.5})\text{Ba}_2\text{Ca}_2\text{Cu}_3\text{O}_{10-\delta}$ were structurally characterized using XRD, Bruker D8 Advance powder diffractometer. The results were carried out at room temperature with $\text{Cu-K}\alpha$ radiation and 2θ ranging from 4 to 70° . From the patterns obtained, lattice parameters and the type of structure were determined for the superconductor samples using interplanar distance and miller indices of the crystal planes for the major phase. The measurements of FTIR spectroscopy were taken using Nicolet iS5 spectrometer with a wavenumber ranging from 700 to 400 cm^{-1} . The spectra browse the influence of nanoparticle's addition on the oxygen phonon modes in $(\text{CuTi})\text{-1223}$ phase

unit cell. The microstructure and grain size of $(\text{CoSiW}_{11})_x/(\text{Cu}_{0.5}\text{Tl}_{0.5})\text{Ba}_2\text{Ca}_2\text{Cu}_3\text{O}_{10-\delta}$ superconducting samples were examined using SEM, AIS 2300 C, proceeded with resolution power of $30\text{ }\mu\text{m}$ at $20\text{ kV} \times 1.5\text{ K}$. The elemental composition analysis was investigated by EDX with Apollo X detector type, accelerated with a voltage of 20 kV .

2.5 Electrical measurement

Electric resistivity measurements were performed using the standard four-probe technique for the prepared samples. The working medium represents a closed cryogenic refrigeration system using liquid nitrogen as a coolant; the results were carried out with the variation of temperature from room temperature down to lower ones ($77\text{ K} \leq T \leq \sim 300\text{ K}$), allowing to determine T_c and zero superconducting transition temperature (T_0). Temperature sensor Platinum–Iridium with $100\text{ }\Omega$ at $0\text{ }^\circ\text{C}$ was used to monitor the temperature of the samples. The cryostat system employed in this measurement is a homemade cryostat connected with liquid nitrogen flow. The dimensions of the samples used in this measurement were about $1.2 \times 0.5 \times 0.4\text{ cm}^3$. The sample was supplied by a constant current of 120 mA by two copper terminals and two copper wires 7 mm apart were connected to the sample using conductive silver paint to measure the voltage. The obtained results were recorded on the PC using CASSY LAB software through CASSY interface. Finally, the critical current density (J_c) was measured also using the four-probe technique at 77 K . The coolant medium used is a liquid nitrogen flow. The current was supplied to the measured samples using a high current power supply source (LD Didactic GmbH) up to $I_{\text{max}} = 20\text{ A}$ in steps of 100 mA for each measurement with $\leq 1\%$ stabilization at full load, while the voltage was recorded using a LEYBOLD DIDACTIC 532 13 microvoltmeter. The samples with dimensions about $1.2 \times 0.4 \times 0.4\text{ cm}^3$ were connected to the copper wires using conductive silver paint.

3 Results and discussions

3.1 POM nanoparticles

The XRD pattern of $\{ \text{CoSiW}_{11} \}$ nanoparticles is depicted in Fig. 1. It shows sharp diffraction peaks around 8.8° , 15.6° , 16.6° , 25.2° , 29° , 34.1° and 39.5° . This result confirms that the compound has high crystallinity, belonging to the tetragonal structure of $P4m^2$ space group without other detectable phases and possessed a Keggin structure [28, 29]. The average crystallite size (D) depends on λ , θ and the full width at half maximum (β). It was determined using Scherrer's equation

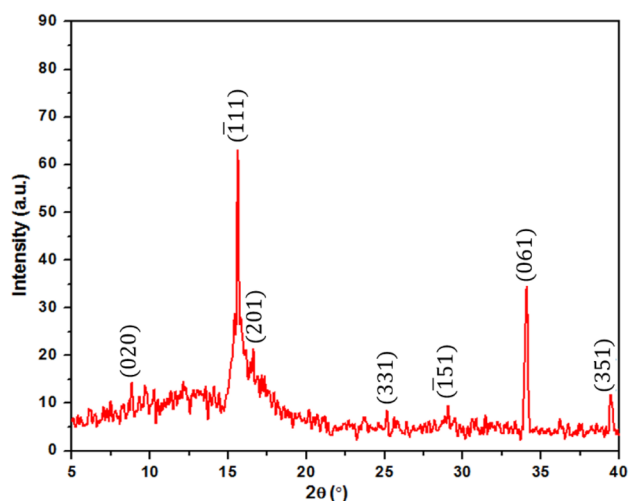


Fig. 1 XRD pattern for {CoSiW₁₁} nanoparticles

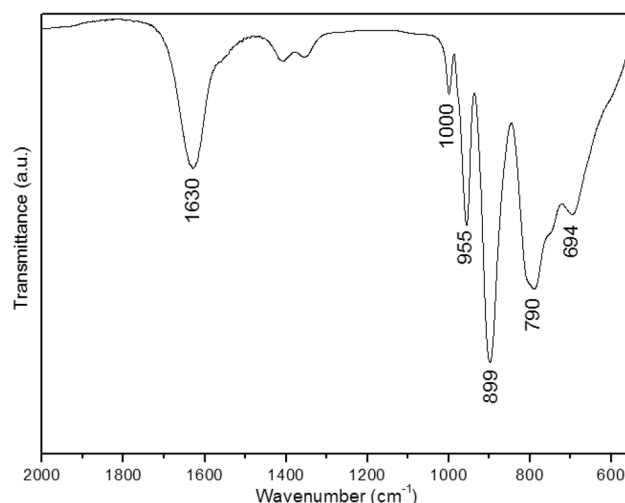


Fig. 2 FTIR spectrum for {CoSiW₁₁} nanoparticles

Table 1 The values of a , c and D (extracted from XRD and TEM results) for {CoSiW₁₁} nanoparticles

Lattice parameters		D (nm)	
a (Å)	c (Å)	XRD	TEM
14.20	12.45	203.9	26.75

$$D = \frac{k\lambda}{\beta \cos \theta} \quad (1)$$

The constant k represents the factor of the tetragonal structure. The high value of D extracted from XRD may be due to the presence of water molecules in the prepared POM [30, 31]. In accordance, Zonnevijlle et al. [32] studied the preparation and characterization of Heteropolytungstates. They listed the structural properties for all polytungstate series concerning the number of cations in the final compound. Thus, the values of lattice parameters (a and c) of our polyoxometalate were conducted and listed in Table 1, as well as those of D .

Figure 2 presents the spectrum of FTIR for {CoSiW₁₁} nanoparticles. The transmission spectrum points out to a strong absorption band ranging from 694 to 1000 cm⁻¹, revealing the characteristic vibrational peaks for Keggin structure. The peak observed at 1630 cm⁻¹ is assigned for the deformation vibrations of water molecule $\delta(\text{H-O-H})$. The presence of anti-symmetric expansion vibration of $\nu_{\text{as}}(\text{Si-O})$, anti-symmetric expansion vibration of $\nu_{\text{as}}(\text{W-O})$, symmetric expansion vibration of $\nu_{\text{s}}(\text{W-O-W})$ and anti-symmetric expansion vibrations of the $\nu_{\text{as}}(\text{W-O-W})$ bridges [33] correspond to wavenumbers 1000, 955, 899 and 790 cm⁻¹, respectively. Compared with the spectrum of Keggin precursor $\text{K}_8[\alpha\text{-SiW}_{11}\text{O}_{39}] \cdot 13\text{H}_2\text{O}$, namely monolacunary, we have observed a nominal change in the peak

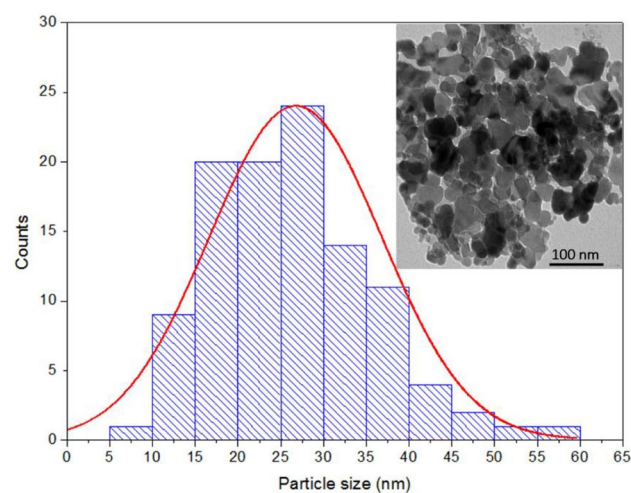


Fig. 3 Particle size distribution and TEM micrograph for {CoSiW₁₁} nanoparticles

position from 800 to 790 cm⁻¹ and an overlap of most of the peaks at the same wavenumber. Furthermore, the spectrum recorded the absence of other anti-symmetric expansion vibrations of $\nu_{\text{as}}(\text{W-O-W})$ bridges at 720 cm⁻¹. It may be related to the change from idealized Cs symmetry to a group symmetry of pseudo-Td point [34]. Al-Oweini et al. [20, 35–37] conducted similar results. In all their studies, they confirmed the purity, chemical bonding and the functional groups of our prepared POM nanoparticles.

Typical TEM image and particle size distribution for {CoSiW₁₁} nanoparticles are depicted in Fig. 3. The microstructure formed exhibits uniform and compact structure of single molecules that are almost of similar and uniform particle size with an average of 26.75 nm. The aggregation of nanoparticles shown in this image represents the irregular

particulate nature of the POM [38]. The presence of a large amount of tungsten prevents the electron beam from entering the spherical assemblies and has thus produced internal dark core spherical fragments [39].

3.2 XRD measurements

The prepared samples were analyzed structurally using XRD measurements. The XRD patterns of $(\text{CoSiW}_{11})_x(\text{Cu}_{0.5}\text{Tl}_{0.5})\text{Ba}_2\text{Ca}_2\text{Cu}_3\text{O}_{10.6}$ phase for all samples are shown in Fig. 4. The diffractogram indicates the formation of a tetragonal crystal

00-038-1402 and JCPDS 00-042-0352 standards can give a help about the peaks of the resulting structures. The cell parameters and the relative volume fraction of (CuTl)-1223 phase were determined using the least-squares method and by comparing the peaks' intensity, respectively [40]. Their values are listed in Table 2. The values of a and c remain approximately constant for all samples, which verify that the impregnated $\{\text{CoSiW}_{11}\}$ nanoparticles remain at the inter-grain boundaries without entering to the matrix of (CuTl)-1223 superconductor phase. The relative volume fraction of $(\text{Cu}_{0.5}\text{Tl}_{0.5})$ -1223 superconducting phase was calculated using the following formula:

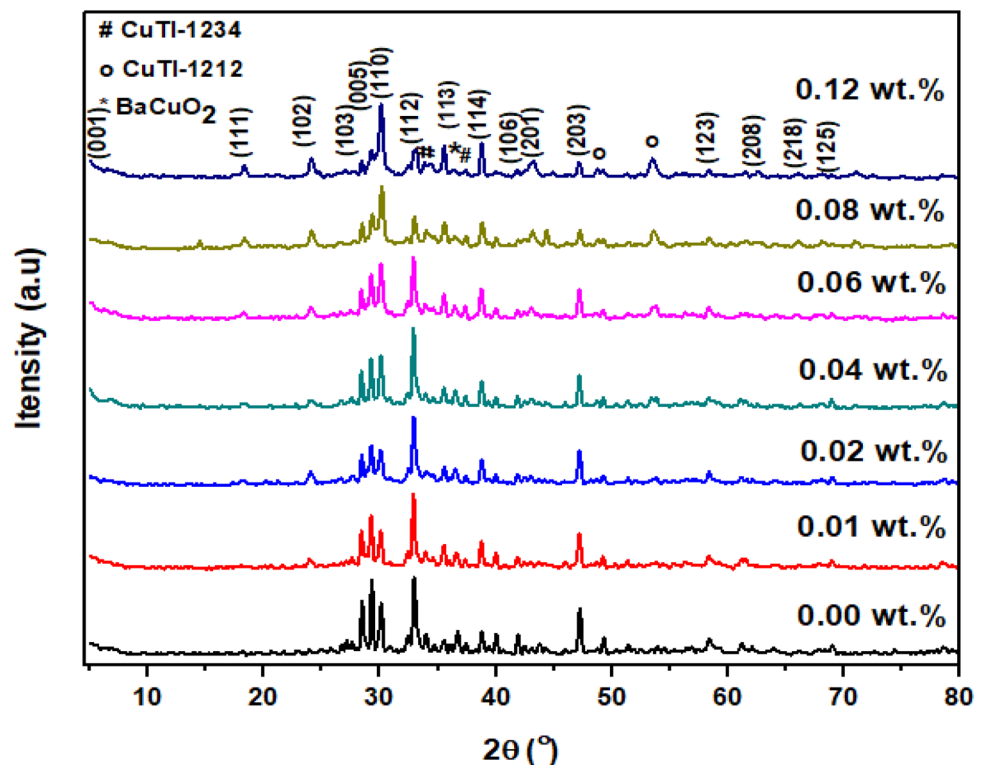
$$[(\text{CuTl})\text{-}1223]\% = \frac{\sum I[(\text{CuTl})\text{-}1223]}{\sum I[(\text{CuTl})\text{-}1223] + \sum I[(\text{CuTl})\text{-}1212] + \sum I[(\text{CuTl})\text{-}1234] + \sum I[\text{BaCuO}_2]} \quad (2)$$

structure with P4/mmm space group, confirming the formation of $(\text{Cu}_{0.5}\text{Tl}_{0.5})$ -1223 superconductor phase. Also, a characteristic peak appeared at $2\theta = 5.1^\circ$ corresponding to (001) crystal plane of the major phase. Moreover, a few additional peaks of small intensity have been observed in XRD scans, revealing the presence of unknown impurities and the formation of other superconductor and non-superconductor phases like (CuTl)-1234, (CuTl)-1212 and BaCuO_2 , respectively. Thus, no change in the peak positions of the major prepared phase is observed. Several ways were used to identify the presence of the compounds: comparing the obtained peaks with literature and using the MAUD program through CIF files. Also, JCPDS

Table 2 The variation of a , c and the relative volume fraction of (CuTl)-1223 phase against $\{\text{CoSiW}_{11}\}$ nanoparticles additions x with $0.00 \leq x \leq 0.12$ wt.%

x (wt.%)	a (Å) (± 0.00278)	c (Å) (± 0.00166)	(CuTl)-1223 (%)
0.00	3.839	15.870	84.54
0.01	3.844	15.872	84.68
0.02	3.844	15.880	92.70
0.04	3.844	15.850	82.98
0.06	3.843	15.877	87.03
0.08	3.832	15.870	86.41
0.12	3.832	15.879	87.38

Fig. 4 XRD pattern for $(\text{CoSiW}_{11})_x(\text{CuTl})\text{-}1223$ superconductor samples for $0.00 \leq x \leq 0.12$ wt.%



where I is the peak intensity of the present phases above the baseline. It increases for $x=0.02$ wt.% to reach its optimum value (92.70%), then decreases till $x=0.04$ wt.% and after that enhances with the enhancement of nanoparticles' concentration to $x=0.12$ wt.%. In general, (CuTl)-1223 superconductor phase is stabilized by the addition of $\{\text{CoSiW}_{11}\}$ nanoparticles. Consequently, this enhancement would be related to the improvement of the connectivity between the grains after the addition of nanoparticles, which acts as pinning centers that fix the vortices [41]. For $x > 0.02$ wt.%, the rate of formation of other phases suppresses that of our prepared phase which may be attributed to the change within the reaction kinetics or within the viscosity of the transient liquid formation [42, 43]. Srour et al. [44] conducted a similar research upon studying the addition effect of BaSnO_3 nanoparticles on $(\text{Cu}_{0.5}\text{Tl}_{0.5})\text{Ba}_2\text{Ca}_2\text{Cu}_3\text{O}_{10.8}$ phase, where the volume fraction was suppressed after a high addition of BaSnO_3 nanoparticles and retarded the formation of the (CuTl)-1223 phase.

3.3 Scanning electron microscope and energy dispersive X-ray

Two SEM micrographs and EDX spectra were taken at two different positions of $(\text{CoSiW}_{11})_x/(\text{Cu}_{0.5}\text{Tl}_{0.5})$ -1223 superconductor phase with $x=0.00, 0.02$ and 0.12 wt.% and are shown in Figs. 5a–c, a'–c', respectively. The pure (CuTl)-1223 sample demonstrates rectangular-shaped plates, indicating the formation of $(\text{Cu}_{0.5}\text{Tl}_{0.5})$ -1223 phase [45] as shown in Fig. 5a, a'. There is also a little number of spherical grains and irregular shapes that refer to the formation of the superconducting $(\text{Cu}_{0.5}\text{Tl}_{0.5})$ -1212 phase [46], $(\text{Cu}_{0.5}\text{Tl}_{0.5})$ -1234 phase and BaCuO_2 non-superconductor composite.

Since the nanoparticles were prepared separately and mixed in (CuTl)-1223 matrix to obtain $(\text{CoSiW}_{11})_x/(\text{Cu}_{0.5}\text{Tl}_{0.5})$ -1223 superconductor composite, the position where these nanoparticles can reside is only between grains and/or on the superconductor grain surfaces. It is clearly noticed that the population of inter-grain connectivity and voids observed in Fig. 5a, a' were reduced after the inclusion of $\{\text{CoSiW}_{11}\}$ nanoparticles, particularly, for $x=0.02$ wt.%. These enhancements among the grains may be due to the presence of nanoparticles at the grain boundaries and the healing-up of voids and microcracks. As a result, this improved the intergranular coupling and inter-grain connectivity by reducing the inter-grain weak links. In contrast, the degradation of the grains presented in Fig. 5c, c' could have resulted from the agglomeration of impregnated nanoparticles at high concentrations ($x=0.12$ wt.%). This could affect the formation rate of (CuTl)-1223 superconductor phase and thus decrease the relative volume fraction.

The EDX spectra were taken at different regions of the specimen, which show the presence of all elements in the final prepared compound. The position of the peaks for Tl, Ba, Ca, O and Cu does not change with the addition of nanoparticles, and the peaks corresponding to W, Si and Co elements appear at $x \geq 0.02$ wt.%. The real atomic percentages for all compositions are recorded in Table 3. These percentage values of Ca, Tl, Ba, O and Cu elements are close to the stoichiometric composition of the $(\text{Cu}_{0.5}\text{Tl}_{0.5})$ -1223 superconductor matrix. Moreover, the enhancement in the atomic percentage of tungsten affirms the regular addition of $\{\text{CoSiW}_{11}\}$ nanoparticles in the prepared phase. Thus, XRD, SEM, EDX and FTIR data show that $\{\text{CoSiW}_{11}\}$ nanoparticles occupy the interstitial spaces among the grains and do not affect the crystal structure of (CuTl)-1223 matrix. Moreover, Fig. 5 is a good representation for showing the grains of superconductor phase and the distribution of $\{\text{CoSiW}_{11}\}$ nanoparticles (in the added nanoparticle's samples), where both SEM images and EDX spectra showed similar results for the same sample as well as the nanoparticles were embedded between the grains.

3.4 FTIR measurements

The FTIR absorption spectra of $(\text{CoSiW}_{11})_x/(\text{CuTl})$ -1223 phase for $x=0.00, 0.01, 0.02, 0.04, 0.08$ and 0.12 wt.% in the wavenumber ranging from 700 to 400 cm^{-1} are shown in Fig. 6a–f. The interesting oxygen phonon modes in the unit cell of (CuTl)-1223 superconductor phase are apical oxygen atoms, CuO_2 planar oxygen atoms and O_8 atoms in the charge reservoir layer [47, 48], which are related to the wavenumber bands from 400 to 540 cm^{-1} , 541 to 600 cm^{-1} and from 670 to 700 cm^{-1} , respectively. Concerning the $(\text{Cu}_{0.5}\text{Tl}_{0.5})\text{Ba}_2\text{Ca}_2\text{Cu}_3\text{O}_{10.8}$ superconductor pure sample, the oxygen phonon modes were observed around i) $419, 429, 439, 448, 458, 468$ and 495 cm^{-1} for apical oxygen of type $\text{Tl-O}_A\text{-Cu}(2)$, ii) 525 and 544 cm^{-1} for apical oxygen of type $\text{Cu}(1)\text{-O}_A\text{-Cu}(2)$, iii) 552 and 576 cm^{-1} for $\text{Cu}(2)\text{-O}_p\text{-Cu}(2)$ planar CuO_2 and finally iv) 669 and 693 cm^{-1} for O_8 atoms.

Among all the impregnated samples with $\{\text{CoSiW}_{11}\}$ nanoparticles, it is obvious from Fig. 6b–f that O_8 modes stayed almost unaltered (669 and 693 cm^{-1}). On the other hand, the slightly softening in most peak positions of both types of apical oxygen modes and also slightly hardening of planar oxygen mode could be attributed to the stresses and strain resulting from the relaxation and compression that would affect the length of the bond between the atoms of (CuTl)-1223 phase matrix. Moreover, the unsystematic change in the peak positions for many vibrational modes may be related to c -axis lengths, observed by XRD results, especially for nanoparticles addition concentrations in the range $0.04 \leq x \leq 0.12$ wt.%. As a conclusion, the impregnated nanoparticles did not interfere with the composition nor

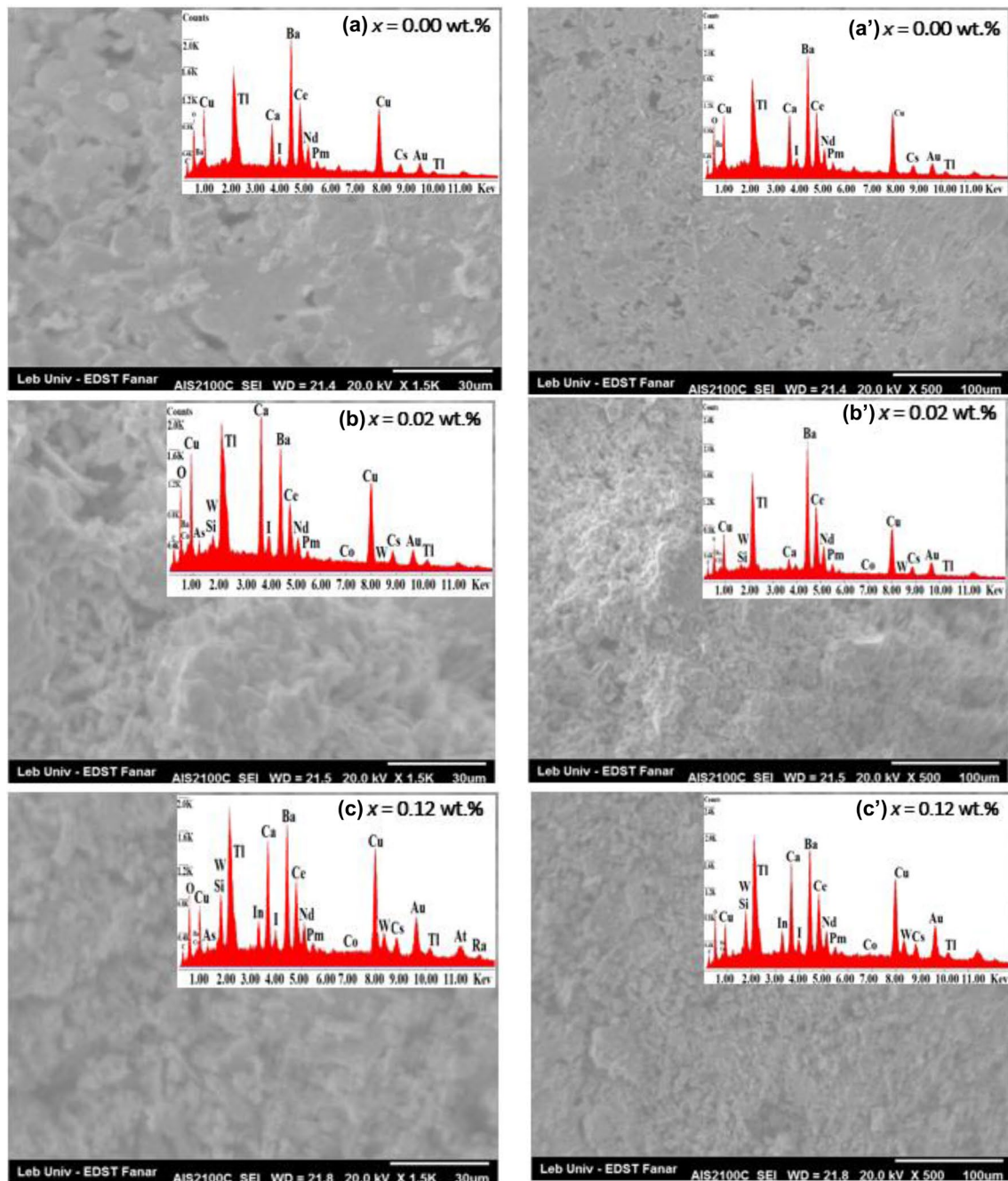


Fig. 5 SEM images inserted with typical EDX spectra of $(\text{CoSiW}_{11})_x/(\text{CuTl})$ -1223 superconductor samples with $x=0.00$ (a, a'), $x=0.02$ (b, b') and $x=0.12$ wt.% (c, c')

changed the stoichiometry of the inter-grain material [44]. From the absorption spectra, the intensity of the O_δ vibrational modes for the impregnated samples was enhanced relative to the pure sample, confirming the existence of oxygen with a higher population through the charge reservoir layer in the doped compound [49]. In addition, a merge may have happened between the peak expected from POM

nanoparticles at 694 cm^{-1} and that of O_δ atoms in superconductor samples at 693 cm^{-1} .

3.5 Resistivity results

The temperature-dependent resistivity measurements of $(\text{CoSiW}_{11})_x/(\text{CuTl})$ -1223 samples ($x=0.00, 0.01, 0.02, 0.04, 0.06, 0.08$ and 0.12 wt.%) in the temperature range from 77

Table 3 Elemental analysis for $(\text{CoSiW}_{11})_x/(\text{CuTl})$ -1223 superconductor samples for $0.00 \leq x \leq 0.12$ wt. %

x (wt.%)	O (%)	Si (%)	Ca (%)	Ba (%)	Co (%)	Cu (%)	W (%)	Tl (%)
0.00	54.07 ± 2.70	0.00 ± 0.0000	12.025 ± 0.60	11.852 ± 0.59	0.00 ± 0.0000	19.308 ± 0.96	0.00 ± 0.0000	2.745 ± 0.137
0.01	53.21 ± 2.66	0.855 ± 0.0427	11.10 ± 0.55	11.41 ± 0.57	0.585 ± 0.0296	19.025 ± 0.95	1.370 ± 0.068	2.43 ± 0.121
0.02	53.06 ± 2.65	0.885 ± 0.0442	11.03 ± 0.55	11.12 ± 0.55	0.605 ± 0.0302	18.875 ± 0.94	1.455 ± 0.072	2.390 ± 0.119
0.04	52.55 ± 2.66	1.333 ± 0.0602	10.64 ± 0.53	11.23 ± 0.55	0.853 ± 0.046	18.396 ± 0.90	2.031 ± 0.099	2.508 ± 0.116
0.06	52.01 ± 2.63	2.275 ± 0.1137	10.51 ± 0.52	11.00 ± 0.55	1.265 ± 0.0632	17.940 ± 0.90	2.710 ± 0.135	2.625 ± 0.081
0.08	51.48 ± 2.75	2.280 ± 0.114	10.12 ± 0.50	9.890 ± 0.49	1.515 ± 0.0757	17.815 ± 0.89	3.940 ± 0.197	2.570 ± 0.078
0.12	51.21 ± 2.56	3.235 ± 0.1619	9.535 ± 0.49	9.77 ± 0.48	2.210 ± 0.0110	17.530 ± 0.87	4.775 ± 0.238	2.135 ± 0.056

to 300 K are shown in Fig. 7. From these curves, all samples show a metallic-like behavior above T_c , followed by a single-step transition. This indicates the presence of good grain connectivity and displays a transition to the superconducting state below T_c . The inset of Fig. 7 displays the first-order derivative of the electrical resistivity ($d\rho/dT$) as a function of T for the pure sample ($x=0.00$ wt.%), where T_c corresponds to the maximum of this derivative, and the single peak indicates that the sample is single phase. The determined values of T_c and T_0 are tabulated in Table 4. It was observed that T_c increases to its highest value (132 K) for $x=0.02$ wt.%, and then it behaves with an unsystematic variation. It decreases until $x=0.04$ wt.% gets its lower value at 115.6 K, followed by an increase for $x=0.06$ wt.% and then a decrease for $x=0.08$ wt.% and finally an increase for $x=0.12$ wt.% to reach $T_c=128.8$ K. This non-monotonic change of these superconducting parameters between $x=0.04$ and 0.12 wt.% could be associated with the multivalence of W that leads to the change in the oxygen content or the inhomogeneous distribution and/or agglomeration of $\{\text{CoSiW}_{11}\}$ nanoparticles at the grain boundaries [50]. It may also be due to the trapping of mobile carriers raised by oxygen vacancy disorder [51, 52]. The enhancement of T_c and T_0 up to $x=0.02$ wt.% could be due to the improvement of volume fraction of (CuTl) -1223 superconductor high T_c phase as determined from XRD results and SEM micrographs as well as due to the reduction in the weak links among the grains. The increase in T_c to 132 K ($x=0.02$ wt.%) may be due to the increase of the c -axis which leads to an increase in the CuO layer [53]. On the other hand, the linear part of the resistivity curves follows the linear equation, Matthiessen rule, which gives the normal state resistivity (ρ_n) as

$$\rho_n = \beta T + \rho_0, \quad (3)$$

where β is the resistivity temperature coefficient and ρ_0 is the residual resistivity [54]. The values of β , ρ_0 , ρ_{room} (at 300 K), and the superconducting transition width ($\Delta T = T_c - T_0$) for all samples, were determined and listed in Table 4. ΔT values are calculated to examine the purity of the prepared samples, where the low value of ΔT recorded for $x=0.02$ wt.% agrees

with the calculated volume fraction in XRD measurements. The variation of ρ_0 and ρ_{room} for $(\text{CoSiW}_{11})_x/(\text{CuTl})$ -1223 as a function of the addition concentration x is also listed in Table 4. The normal state resistivity ρ_{room} is noticed as a measure of the disorder of $\{\text{CoSiW}_{11}\}$ nanoparticles at grain boundaries; hence the increase in ρ_{room} for $x > 0.08$ is due to the enhancement of the secondary phases, which increases the number of scattering centers and reduces the inter-granular coupling [55]. The lower value of ρ_0 corresponds to the higher value of T_c , indicating the decrease of carrier-impurities scattering and that the samples are of high quality with fewer defects [56]. In Table 4, the decrease of β values in the samples with high T_c values may be due to the increase in the carrier-concentrations.

3.6 I–V measurements

The ability of the prepared superconducting samples to hold current is analyzed using the transport critical current density measurements at a low temperature (77 K). The variation of the electric field (E) as a function of the current density (J) for $(\text{CoSiW}_{11})_x/(\text{CuTl})$ -1223 phase with $x=0.00, 0.01, 0.02, 0.06$ and 0.12 wt.% is shown in Fig. 8. The obtained values of J_c are tabulated in Table 5. The behavior of the curves can be interpreted as follows: The current in the first portion is not large enough to cause vortex pair unbinding, which implies that $V(J)=0$. Thus, the system is resistanceless [57]. In the second portion of the curve, where the values of voltage are low, the free vortices below T_c are created due to a finite penetration depth which is resolved by a thermally assisted flux flow. In the nonlinear portion, the voltage drop appears at a certain value of applied current I_c . This mechanism is described by flux creep, where the Lorentz force (FL) is equal to the Pinning force (FP). The last portion exhibits the increase in the linear curve; this is due to the vortex pair unbinding caused by the strong Lorentz force, ($\text{FL} > \text{FP}$), discussed by flux flow explanations. The variation of porosity, oxygen deficiency, crystallinity, grain morphology, the relative volume fraction and many other factors may affect J_c as well as T_c .

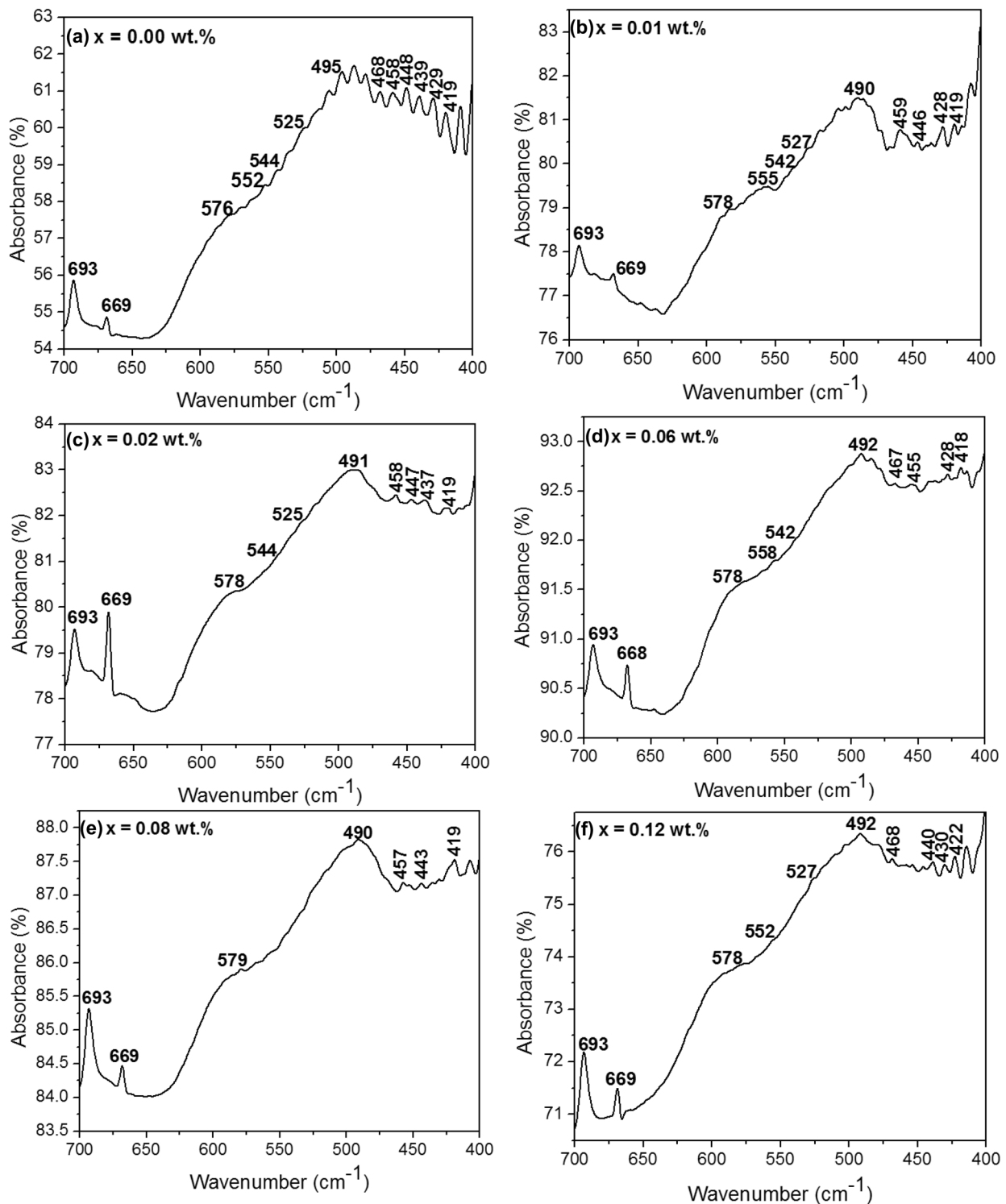


Fig. 6 Fourier transform infrared (FTIR) spectra for $(\text{CoSiW}_{11})_x/(\text{CuTl})$ -1223 superconductor samples with $x=0.00$ (a), 0.01 (b), 0.02 (c), 0.06 (d), 0.08 (e) and 0.12 wt.% (f)

It is seen from Table 5 that the values of J_c decrease with the increase of nanoparticle concentration x from $x=0.01$ up to 0.12 wt.%. The suppression in the J_c values, despite the improvement of T_c and phase formation, especially for

$x=0.02$ wt.%, may be due to the increment of the grain boundary resistance or the presence/growth of minor superconductor and non-superconductor phases impurities. But the high retrogression of J_c for $x=0.06$ and 0.12 wt.% could

Fig. 7 The electrical resistivity dependence on temperature for $(\text{CoSiW}_{11})_x/(\text{CuTl})$ -1223 superconductor samples for $0.00 \leq x \leq 0.12$ wt.%. The inset graph shows the variation of $(d\rho/dT)$ versus T for $x=0.00$ wt.%

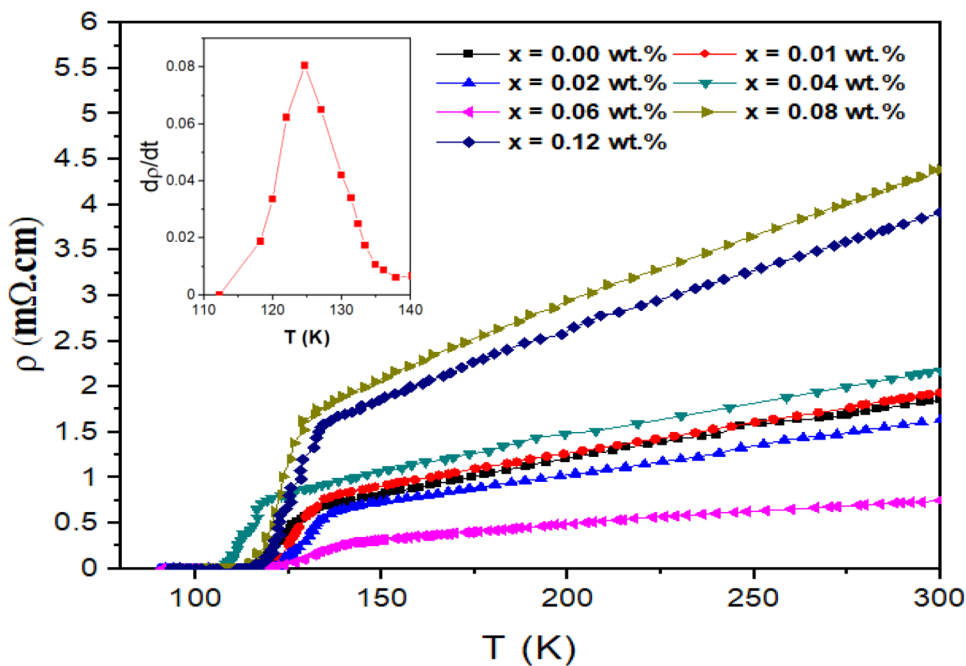


Table 4 The variation of T_c , T_0 , ρ_0 , ρ_{room} , β and ΔT against $\{\text{CoSiW}_{11}\}$ nanoparticles additions on (CuTl) -1223 superconductor samples for $0.00 \leq x \leq 0.12$ wt.%

x (wt. %)	T_c (K)	T_0 (K)	ρ_0 (mΩ cm)	ρ_{room} (mΩ cm)	β (mΩ cm K ⁻¹)	ΔT (K)
0.00	124.6	114.4	0.029	1.859	0.0060	10.2
0.01	125.0	115.8	0.044	1.934	0.0063	9.20
0.02	132.0	124.7	0.015	1.635	0.0054	7.30
0.04	115.6	107.0	0.020	2.180	0.0072	8.60
0.06	126.6	117.6	0.012	1.152	0.0038	9.00
0.08	123.5	113.8	0.035	4.385	0.0145	9.70
0.12	128.8	116.1	0.102	3.912	0.0090	12.7

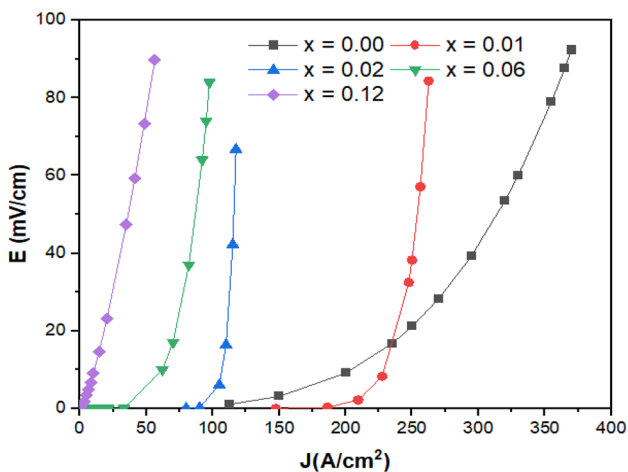


Fig. 8 $(E-J)$ curves for $(\text{CoSiW}_{11})_x/(\text{CuTl})$ -1223 superconductor samples with $x=0.00, 0.01, 0.02, 0.06$ and 0.12 wt.%

Table 5 The variation of J_c , n and U against $\{\text{CoSiW}_{11}\}$ nanoparticles' additions for $(\text{CoSiW}_{11})_x/(\text{CuTl})$ -1223 superconductor samples with $x=0.00, 0.01$ and 0.02 wt.%

x (wt.%)	0.00	0.01	0.02	0.06	0.12
J_c (A/cm ²)	255.35	220.65	102.04	74.44	12.889
n	3.7570	16.209	21.299	4.674	1.328
$U \times 10^{-2}$ (eV)	3.1079	13.408	17.619	3.866	1.0985

be due to large agglomeration of $\{\text{CoSiW}_{11}\}$ nanoparticles among the grains, decrement of volume fraction and the increasing growth of impurity content. The obtained curves are investigated through the following relation:

$$E = \gamma J^n, \tag{4}$$

where γ and n are material dependent constants. The n values, index of transition, describe the homogeneity of a superconductor and can be calculated from the slope of $\ln(E)$ in terms of $\ln(J)$. It is important to note that the higher the n values, the more homogeneous the prepared samples and the higher their quality. The highest n value of 21.299 observed in the $x=0.02$ wt.% sample reflects these aforementioned properties and is consistent with the lowest residual resistivity value $\rho_0=0.015$ (m Ω cm) and the highest T_c value of 132 K observed in this sample. Also, it is related to the pinning potential U according to the following equation [58]:

$$n = \frac{U}{Tk_B} \quad (5)$$

The values of n and U are also listed in Table 5. There is the proportionality of n and U with respect to the addition content of x (wt.%). Thus, with the addition of $\{\text{CoSiW}_{11}\}$ nanoparticles, the superconductor homogeneity becomes greater.

3.7 Excess conductivity analysis

Figure 9a–f presents the normalized excess conductivity $\Delta\sigma/\sigma_{\text{room}}$ versus the reduced temperature t in \ln – \ln plot for $(\text{CoSiW}_{11})_x/(\text{CuTl})$ -1223 phase for $x=0.00, 0.01, 0.02, 0.06, 0.08$ and 0.12 wt.%. It is clearly observed that the plotted curves are divided into four unlike regions (Sw, 2D, 3D and Cr).

According to Aslamazov–Larkin (AL) model [8], the excess conductivity $\Delta\sigma$ is defined as follows:

$$\sigma = \sigma_m(T) - \sigma_n(T) \frac{1}{\rho_m(T)} - \frac{1}{\rho_E(T)}, \quad (6)$$

where $\rho_m(T)$ is the measured resistivity for each temperature T . The values of $\rho_n(T)$ were determined from the linear fit of dc-resistivity curves for $T \geq 2T_c$.

According to AL model, the normalized excess conductivity is given as follows:

$$\frac{\sigma}{\sigma_{\text{room}}} = Ct^Z, \quad (7)$$

where $t = \frac{T-T_c}{T_c}$ is the reduced temperature and Z is the conductivity exponent [59], which has the following values:

$$Z = \begin{cases} -0.3 & \text{for (Cr) fluctuations} \\ -0.5 & \text{for (3D) fluctuations} \\ -1 & \text{for (2D) fluctuations} \\ -3 & \text{for (Sw) fluctuations} \end{cases}$$

On the other hand, the constant C is the temperature-independent amplitude and is given by the following equations in 3D and 2D, respectively [3, 4]:

$$C_{3D} = \frac{e^2}{32\hbar\xi_c(0)\sigma_{\text{room}}} \quad (8)$$

and

$$C_{2D} = \frac{e^2}{16\hbar d\sigma_{\text{room}}}, \quad (9)$$

where $\xi_c(0)$ parameter represents the zero-temperature coherence length along the c -axis while the effective layer thickness of the 2D is d .

The interlayer coupling (J), Fermi velocity (v_F) and Fermi energy (E_F) were calculated as follows:

$$J = \left[\frac{\xi_c(0)}{d} \right]^2 \quad (10)$$

$$v_F = \frac{3.5\pi k_B T_c \xi_c(0)}{2\hbar} \quad (11)$$

$$E_F = (m^* v_F^2)/2, \quad (12)$$

where k_B is the Boltzmann's constant and $m^*=10.m_0$ is the electron effective mass [60]. The four different regions are linearly fitted and also the conductivity exponent Z is calculated from the slope. At the junction of various thermally activated processes, three crossover temperatures are found, i.e., $T_G=T_{3D-Cr}$, T_{2D-3D} and T_{Sw-2D} . The T_G is the crossover temperature of Ginzburg–Landau regime with three-dimensional conductivity regimes, the T_{2D-3D} is the crossover temperature of 3D conductivity regime with 2D conductivity regimes and the T_{Sw-2D} is the crossover temperature of 2D conductivity regime critical fluctuations conductivity region.

The crossover temperatures are determined from the intersection between the linear parts of the different regions. The crossover temperatures for the samples are listed in Table 6.

Concerning the first region Sw, which corresponds to high temperature, the excess conductivity reduces sharply with Z_{Sw} -values starting from -2.867 to -3.113 , denoting the prevalent role of short-wave fluctuation [61]. A crossover between the mean-field region and the short-wave fluctuations is detected at a temperature T_{Sw-2D} above T_c by decreasing the temperature. The existence of the 2D and 3D fluctuations are clearly observed in the graphs with the conductivity exponents varying as $-0.972 \leq Z_{2D} \leq -1.151$ and $-0.487 \leq Z_{3D} \leq -0.606$, respectively. In the 2D region, the charge carriers move in the conducting CuO_2 planes resulting from the layered structure which characterizes the HTSCs, while in the 3D region, they move between the molecular planes and they are more influenced by thermal fluctuations. This means that the charge carriers tend to displace more freely in the global crystal before they make pairs. In the critical region, the conductivity exponent varies

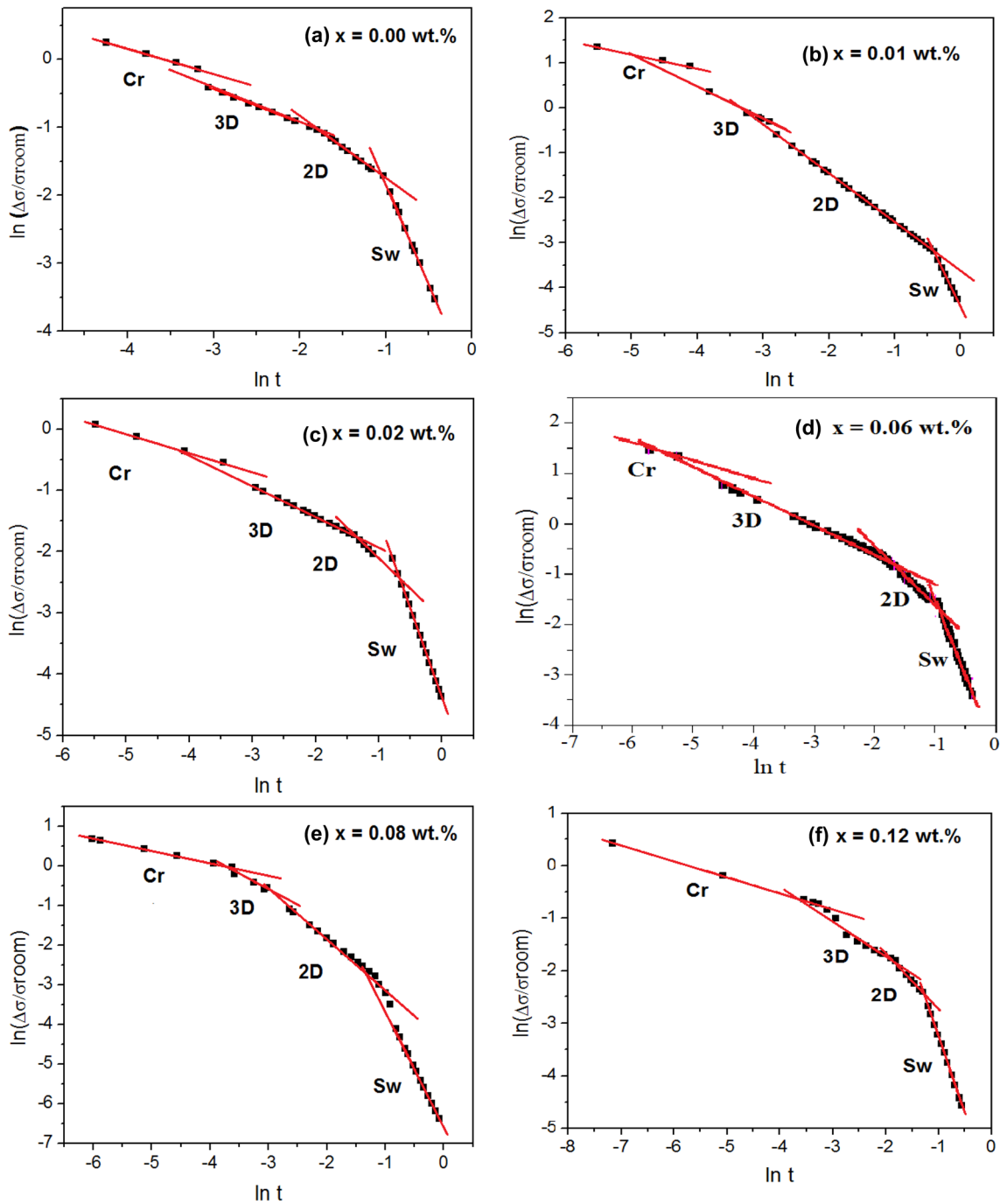


Fig. 9 Normalized excess conductivity versus reduced temperature t in \ln - \ln plot for $(\text{CoSiW}_{11})_x/(\text{CuTi})$ -1223 superconductor samples for $x=0.00, 0.01, 0.02, 0.06, 0.08$ and 0.12 wt.%

as $-0.294 \leq Z_{\text{Cr}} \leq -0.37$. Hence, the order parameter fluctuations become comparable in magnitude to the order parameter value [62].

The values of $\zeta_c(0)$, d and I are calculated according to Eqs. (8)–(10), respectively; the values of v_F and E_F are calculated from Eqs. (11) and (12) and all values are listed in Table 7. The increase in the coherence length along the

c -axis and the effective layer thickness, with increasing the concentration of $\{\text{CoSiW}_{11}\}$ nanoparticles, confirm that the inter-planar coupling is enhanced in our samples. The values of v_F and E_F are increased with increasing $\{\text{CoSiW}_{11}\}$ concentration; this confirms that the addition of $\{\text{CoSiW}_{11}\}$ promotes the Josephson junction-like coupling between CuO_2 planes. Moreover, the values of I are less than one, which

Table 6 Variation of the crossover temperatures with $\{\text{CoSiW}_{11}\}$ nanoparticles' additions

x (wt.%)	$T_{\text{Sw-2D}}$ (K)	$T_{\text{2D-3D}}$ (K)	$T_{\text{3D-Cr}}=T_{\text{G}}$ (K)
0.00	170.18	146.78	125.57
0.01	206.95	130.00	125.27
0.02	200.67	165.66	133.97
0.06	176.10	156.65	126.61
0.08	156.82	128.46	125.48
0.12	164.11	147.43	129.92

confirms the low coupling between CuO_2 planes and the crossover between 3 and 2D regions [63].

The variance of the microscopic parameters measured from the FIC study is following the experimental finding in the FTIR measurements, where the higher oxygen population in the charge reservoir layer increases the density of the charging carriers in the CuO_2 conducting planes. The optimal density of mobile charging carriers in the conducting CuO_2 planes results in an improvement in the material's grain size, while also increasing the inter-grain connectivity and explaining the overall enhancement of superconductivity after introducing nanoparticles $\{\text{CoSiW}_{11}\}$ to the (CuTl) -1223 superconductor.

4 Conclusion

The effect of $\{\text{CoSiW}_{11}\}$ nanoparticles' addition on the superconducting properties as well as the phase formation of (CuTl) -1223 matrix was thoroughly studied. We synthesized $(\text{CoSiW}_{11})_x/(\text{CuTl})$ -1223 phase with $0.00 \leq x \leq 0.12$ wt.% successfully by a single-step solid-state reaction technique at normal pressure. The lower nano-addition, $0.0 \leq x \leq 0.02$ wt.%, increased the volume fraction of $(\text{Cu}_{0.5}\text{Tl}_{0.5})$ -1223 superconductor major phase up to its maximum value for $x = 0.02$ wt.%; then it was reduced with the further increase

of x , as indicated by XRD results. The lattice parameters remain almost constant, thus indicating that the nanoparticles did not enter the unit cell; however, they exist only at the grain boundaries. The SEM micrographs show the formation of (CuTl) -1223 phase, which was enhanced after the addition of $\{\text{CoSiW}_{11}\}$ nanoparticles for $x = 0.02$ wt.%, thus confirming the results of relative volume fraction. Moreover, the elemental analyses of the samples, recorded by EDX, show that the mass percentage of all elements is closer to the stoichiometric composition of the host superconductor $(\text{Cu}_{0.5}\text{Tl}_{0.5})$ -1223 matrix as well as that of nanoparticles' compound. The latter indication was also confirmed in the FTIR results, where the position of O_δ modes did not change and the fact that both types of the apical oxygen modes and the planar oxygen modes are slightly softened and hardened, respectively. Furthermore, the superconducting transition temperature, T_c , increases up to its maximum value for $x = 0.02$ wt.%, then decreases with a further increase of x , as indicated in electrical resistivity results. Although most of the superconducting parameters were improved after the addition of $\{\text{CoSiW}_{11}\}$ nanoparticles, the critical current density gave wondrous results. The values of J_c decrease with the increase of nanoparticle's addition up to $x = 0.12$ wt.%. Finally, the conductivity exponents obtained from the plot of the excess conductivity $\Delta\sigma/\sigma_{\text{room}}$ with a reduced temperature t were about -0.3 , -0.5 , -1.0 and -3 , corresponding to the fluctuation's regions Cr, 3D, 2D and Sw, respectively. Correspondingly, the values coincide with the theoretical predictions. Moreover, the enhancement of the inter-planar coupling was confirmed from the increase in the coherence length along the c -axis, and the effective layer thickness as the added concentration of $\{\text{CoSiW}_{11}\}$ nanoparticles increased. Furthermore, the Josephson junction, similar to the coupling between CuO_2 planes, was also promoted by the increase of v_F and E_F values. Finally, all the results obtained under our preparation conditions revealed that the sample with $x = 0.02$ wt.% had the best superconducting parameters.

Table 7 Superconducting parameters of $(\text{CoSiW}_{11})_x/(\text{CuTl})$ -1223 phase with $0.00 \leq x \leq 0.12$ wt.% conducted from excess conductivity measurements

x (wt.%)	$Z(\text{Sw})$	$Z(\text{2D})$	$Z(\text{3D})$	$Z(\text{Cr})$	$\zeta_c(0)$ (Å)	d (Å)	$I \times 10^{-2}$	$v_F \times 10^6$ (m/s)	E_F (eV)
0.00	-3.04	-0.97	-0.49	-0.37	9.69	44.30	4.780	0.087	0.218
0.01	-2.89	-1.08	-0.57	-0.31	10.7	111.6	0.92	0.096	0.264
0.02	-2.91	-1.01	-0.50	-0.31	14.2	57.47	6.148	0.135	0.521
0.04	-2.87	-1.00	-0.48	-0.31	19.5	129.2	2.291	0.162	0.746
0.06	-3.11	-1.09	-0.53	-0.30	5.8	25.75	5.055	0.053	0.080
0.08	-3.04	-1.15	-0.60	-0.29	36.2	418.6	0.747	0.321	2.920
0.12	-2.89	-1.04	-0.52	-0.29	46.6	255.9	3.315	0.429	5.240

References

1. M.H. Pu, W.H. Song, B. Zhao, X.C. Wu, Y.P. Sun, J.J. Du, J. Fang, *Phys. C* **361**, 181 (2001)
2. H. Ihara, K. Tanaka, Y. Tanaka, A. Iyo, N. Terada, M. Tokumoto, F. Tateai, M. Kawamura, K. Ishida, S. Miyashita, T. Watanabe, *Phys. B* **284–288**, 1085 (2000)
3. H. Ihara, K. Tanaka, Y. Tanaka, A. Iyo, N. Terada, M. Tokumoto, M. Ariyama, I. Hase, A. Sundaresan, N. Hamada, S. Miyashita, K. Tokiwa, T. Watanabe, *Phys. C* **341–348**, 487 (2000)
4. M. Mumtaz, S.M. Hasnain, A.A. Khurram, N.A. Khan, *J. Appl. Phys.* **109**, 023906 (2011)
5. H. Ihara, K. Tokiwa, K. Tanaka, T. Tsukamoto, T. Watanabe, H. Yamamoto, A. Iyo, M. Tokumoto, M. Umeda, *Phys. C* **282–287**, 957 (1997)
6. I. Qasim, M. Waqee-ur-Rehman, M. Mumtaz, G. Hussain, K. Nadeem, K. Shehzad, *J. Magn. Magn. Mater.* **403**, 60 (2016)
7. N.H. Mohammed, *Phys. C* **485**, 95 (2013)
8. L.G. Aslamasov, A.I. Larkin, *Phys. Lett. A* **26**, 238 (1968)
9. Y. Jia, P. Cheng, L. Fang, H. Luo, H. Yang, C. Ren, L. Shan, C. Gu, H.-H. Wen, *Appl. Phys. Lett.* **93**, 032503 (2008)
10. S. Rajput, S. Chaudhary, *J. Mater.* **2013**, 1 (2013)
11. G.H. Lee, R. Abd-Shukor, *AIP Conf. Proc.* **1528**, 292 (2013)
12. K.T. Lau, S.Y. Yahya, R. Abd-Shukor, *J. Appl. Phys.* **99**, 123904 (2006)
13. M.M. Elokr, R. Awad, A. Abd El-Ghany, A. Abou Shama, A. Abd El-wanis, *J. Supercond. Nov. Magn.* **24**, 1345 (2011)
14. M. Mumtaz, Z. Iqbal, M.R. Hussain, L. Ali, M. Waqee-ur-Rehman, M. Saqib, *J. Supercond. Nov. Magn.* **31**, 1315 (2018)
15. N. Hassan, N.A. Khan, *J. Alloy. Compd.* **471**, 39 (2009)
16. N.H. Mohammed, A.I. Abou-Aly, I.H. Ibrahim, R. Awad, M. Rekaby, *J. Alloy. Compd.* **486**, 733 (2009)
17. N.A. Khan, M. Irfan, *Phys. C* **468**, 2341 (2008)
18. L. Youssef, G. Younes, R. Al-Oweini, *J. Taibah Univ. Sci.* **13**, 274 (2019)
19. F. Yahya, H. El-Rassy, G. Younes, R. Al-Oweini, *Int. J. Environ. Anal. Chem.* **99**, 1375 (2019)
20. R. Al-Oweini, B.S. Bassil, M. Itani, D.B. Emiroğlu, U. Kortz, *Acta Cryst. C* **74**, 1390 (2018)
21. M. Natali, I. Bazzan, S. Goberna-Ferrón, R. Al-Oweini, M. Ibrahim, B.S. Bassil, H. Dau, F. Scandola, J.R. Galán-Mascarós, U. Kortz, A. Sartorel, I. Zaharieva, M. Bonchio, *Green Chem.* **19**, 2416 (2017)
22. A. Bijelic, C. Molitor, S.G. Mauracher, R. Al-Oweini, U. Kortz, A. Rompel, *ChemBioChem* **16**, 233 (2015)
23. R. Al-Oweini, A. Sartorel, B.S. Bassil, M. Natali, S. Berardi, F. Scandola, U. Kortz, M. Bonchio, *Angew. Chem. Int. Ed.* **53**, 11182 (2014)
24. R. Al-Oweini, S. Aghyarian, H. El-Rassy, *J. Sol–Gel Sci. Technol.* **61**, 541 (2012)
25. N.E. Ghouch, R. Al-Oweini, R. Awad, *Mater. Res. Express* **6**, 116001 (2019)
26. N.E. Ghouch, R. Al-Oweini, R. Awad, *Appl. Phys. A* **12**, 1 (2019)
27. A. Müller, L. Dloczik, E. Diemann, M.T. Pope, *Inorg. Chim. Acta* **257**, 231 (1997)
28. T. Huang, N. Tian, Q. Wu, Y. Yan, W. Yan, *Mater. Chem. Phys.* **165**, 34 (2015)
29. N. Tian, M. Zhu, Q. Wu, W. Yan, A.B. Yaroslavtsev, *Mater. Lett.* **115**, 165 (2014)
30. F.J. Berry, G.R. Derrick, M. Mortimer, *Polyhedron* **68**, 17 (2014)
31. M.J. da Silva, L.C. de Andrade-Leles, R. Natalino, S.O. Ferreira, N.C. Coronel, *Catal. Lett.* **148**, 1202 (2018)
32. Frans. Zonnevijlle, C. M. Tourne, and G. F. Tourne, *Inorg. Chem.* **21**, 2742 (1982).
33. Z. Li, W. Li, X. Li, F. Pei, X. Wang, H. Lei, *J. Inorg. Biochem.* **101**, 1036 (2007)
34. M. Sadakane, D. Tsukuma, M.H. Dickman, B.S. Bassil, U. Kortz, M. Capron, W. Ueda, *Dalton Trans.* **26**, 2833 (2007)
35. R. Al-Oweini, H. El-Rassy, *J. Mol. Struct.* **919**, 140 (2009)
36. R. Al-Oweini, B.S. Bassil, T. Palden, B. Keita, Y. Lan, A.K. Powell, U. Kortz, *Polyhedron* **52**, 461 (2013)
37. R. Al-Oweini, B.S. Bassil, J. Friedl, V. Kottisch, M. Ibrahim, M. Asano, B. Keita, G. Novitchi, Y. Lan, A. Powell, U. Stimming, U. Kortz, *Inorg. Chem.* **53**, 5663 (2014)
38. T.A.G. Duarte, A.C. Estrada, M.M.Q. Simões, I.C.M.S. Santos, A.M.V. Cavaleiro, M.G.P.M.S. Neves, J.A.S. Cavaleiro, *Catal. Sci. Technol.* **5**, 351 (2015)
39. M. Saeidifar, H. Mirzaei, N. Ahmadi-Nasab, H. Mansouri-Torshizi, *J. Mol. Struct.* **1148**, 339 (2017)
40. W. Abdeen, A. El-Tahan, R. Awad, A.I. Abou-Aly, E.M. El-Maghraby, A. Khalaf, *Appl. Phys. A* **122**, 574 (2016)
41. K. Kocabaş, M. Gökçe, M. Çiftçioğlu, Ö. Bilgili, *J. Supercond. Novel Magn.* **23**, 397 (2010)
42. M. Imran, M. Z. Khan, M. Waqee-Ur-Rehman, A. Ullah, S. Ahmed, K. Nadeem, and M. Mumtaz, *J. Low Temp. Phys.* (2020)
43. M. Me, Barakat and K. Habanjar, *J Adv Ceram* **6**, 100 (2017)
44. A. Srour, R. Awad, W. Malaeb, M.M.E. Barakat, *J. Low Temp. Phys.* **189**, 217 (2017)
45. R. Awad, A.I. Abou-Aly, S. Isber, W. Malaeb, *J. Phys.* **43**, 474 (2006)
46. P. Badica, A. Iyo, A. Crisan, Y. Ishiura, A. Sundaresan, H. Ihara, *Supercond. Sci. Technol.* **15**, 964 (2002)
47. H. Salamati, P. Kameli, *Solid State Commun.* **125**, 407 (2003)
48. V.P.S. Awana, S.K. Malik, W.B. Yelon, C.A. Cardoso, O.F. de Lima, A. Gupta, A. Sedky, A.V. Narlikar, *Phys. C* **338**, 197 (2000)
49. M. Mumtaz, N.A. Khan, S.M. Hasnain, F. Ashraf, *J. Supercond. Nov. Magn* **25**, 2291 (2012)
50. N.E. Ghouch, R. Al-Oweini, R. Awad, *J. Low Temp. Phys.* **200**, 62 (2020)
51. A. Mellekh, M. Zouaoui, F. Ben-Azzouz, M. Annabi, M. Ben-Salem, *Solid State Commun.* **140**, 318 (2006)
52. J. Zhang, F. Liu, G. Cheng, J. Shang, J. Liu, S. Cao, Z. Liu, *Phys. Lett. A* **201**, 70 (1995)
53. K.A. Jasim, L.A. Mohammed, *J. Phys. Conf. Ser.* **1003**, 012071 (2018)
54. Y. Slimani, E. Hannachi, M.K. Ben Salem, A. Hamrita, M.B. Salem, F.B. Azzouz, *J. Supercond. Nov. Magn.* **28**, 3001 (2015)
55. A. Nishida, C. Taka, I. Shigeta, *Phys. C* **392–396**, 349 (2003)
56. A.K. Ghosh, S.K. Bandyopadhyay, P. Barat, P. Sen, A.N. Basu, *Phys. C* **255**, 319 (1995)
57. T.M. Katona, S.W. Pierson, *Phys. C* **270**, 242 (1996)
58. S.E. Mousavi Ghahfarokhi, M. Zargar Shoushtari, *Phys. B Condens. Matter* **405**, 4643 (2010)
59. A.K. Pradhan, S.B. Roy, P. Chaddah, C. Chen, B.M. Wanklyn, *Phys. Rev. B* **50**, 7180 (1994)
60. I. Van Driessche, A. Buekenhoudt, K. Konstantinov, E. Bruneel, S. Hoste, *Appl. Supercond.* **4**, 185 (1996)
61. L. Reggiani, R. Vaglio, A.A. Varlamov, *Phys. Rev. B* **44**, 9541 (1991)
62. C.J. Lobb, *Phys. Rev. B* **36**, 3930 (1987)
63. A.I. Abou-Aly, R. Awad, I.H. Ibrahim, W. Abdeen, *Solid State Commun.* **149**, 281 (2009)

Publisher's Note Springer Nature remains neutral with regard to jurisdictional claims in published maps and institutional affiliations.

Affiliations

Abbass Nasser¹ · Ali Srour¹ · Nour El Ghouch² · Walid Malaeb¹ · Rami Al-Oweini³ · Ramadan Awad¹

¹ Department of Physics, Faculty of Science,
Beirut Arab University, P.O. Box 11-5020,
Riad El-Solh, Beirut 1107 2809, Lebanon

² Department of Chemistry, Faculty of Science,
Beirut Arab University, P.O. Box 11-5020,
Riad El-Solh, Beirut 1107 2809, Lebanon

³ Faculty of Arts and Sciences, Kamal A. Shair Central
Research Science Laboratory, American University of Beirut,
P.O. Box 11-0236, Riad El-Solh, Beirut 1107 2020, Lebanon